Beyond Solid Solution High-Entropy Alloys

Tailoring Magnetic Properties via Spinodal Decomposition

Rao, Ziyuan; Dutta, Biswanath; Körmann, Fritz; Lu, Wenjun; Zhou, Xuyang; Liu, Chang; da Silva, Alisson Kwiatkowski; Wiedwald, Ulf; Spasova, Marina; Farle, Michael

DOI
10.1002/adfm.202007668

Publication date
2021

Document Version
Final published version

Published in
Advanced Functional Materials

Citation (APA)
Rao, Z., Dutta, B., Körmann, F., Lu, W., Zhou, X., Liu, C., da Silva, A. K., Wiedwald, U., Spasova, M., Farle, M., Ponge, D., Gault, B., Neugebauer, J., Raabe, D., & Li, Z. (2021). Beyond Solid Solution High-Entropy Alloys: Tailoring Magnetic Properties via Spinodal Decomposition. *Advanced Functional Materials*, *31*(7), Article 2007668. https://doi.org/10.1002/adfm.202007668

ADVANCED FUNCTIONAL MATERIALS
www.afm-journal.de

Beyond Solid Solution High-Entropy Alloys: Tailoring Magnetic Properties via Spinodal Decomposition

Ziyuan Rao, Biswanath Dutta, Fritz Körmann, Wenjun Lu, Xuyang Zhou, Chang Liu, Alisson Kwiatkowski da Silva, Ulf Wiedwald, Marina Spasova, Michael Farle, Dirk Ponge, Baptiste Gault, Jörg Neugebauer, Dierk Raabe, and Zhiming Li**

Since its first emergence in 2004, the high-entropy alloy (HEA) concept has aimed at stabilizing single- or dual-phase multi-element solid solutions through high mixing entropy. Here, this strategy is changed and renders such massive solid solutions metastable, to trigger spinodal decomposition for improving the alloys' magnetic properties. The motivation for starting from a HEA for this approach is to provide the chemical degrees of freedom required to tailor spinodal behavior using multiple components. The key idea is to form Fe-Co enriched regions which have an expanded volume (relative to unconstrained Fe-Co), due to coherency constraints imposed by the surrounding HEA matrix. As demonstrated by theory and experiments, this leads to improved magnetic properties of the decomposed alloy relative to the original solid solution matrix. In a prototype magnetic FeCoNiMnCu HEA, it is shown that the modulated structures, achieved by spinodal decomposition, lead to an increase of the Curie temperature by 48% and a simultaneous increase of magnetization by 70% at ambient temperature as compared to the homogenized single-phase reference alloy. The findings thus open a pathway for the development of advanced functional HEAs.

1. Introduction

High-entropy alloys (HEAs), composed of multi-principal elements, have shown great potential for achieving excellent mechanical and functional properties,[1] for example, a good combination of strength and ductility,[1e,h] high creep resistance[2] and tunable magnetic behavior.[1j] The high-entropy effect was originally proposed to stabilize single- or dual-phase solid solutions, enabling high lattice distortion, to increase the lattice friction for dislocation glide. In this context, phase decomposition has been seen as an unwanted phenomenon, as phase separation leads to a state of lower atomic mixing and hence lower lattice distortion.[3] Despite this original preference for designing single-phase HEAs, phase decomposition happens in most single-phase solid–solution HEAs after prolonged annealing at medium temperatures,[4] and the focus in the field is progressively shifting toward exploiting rather than counteracting the metastability of these alloys. The reason for this shift in strategy is that additional phases may offer multiple advantages, ranging from high interface density to beneficial properties of the phases that are formed. The practically unbounded compositional space offered by the HEAs concept, particularly when dropping the tenet of a homogenous solid solution, provides numerous possibilities for exploiting complex phase transformation sequences compared to conventional alloys. However, it is still unclear whether phase decompositions can be exploited to truly improve the properties of HEAs, which in turn would provide ample room for further well-targeted thermodynamics and kinetics investigations. Phase decomposition has indeed been frequently observed in HEAs, however, mostly creating side effects outside of the target mechanical and magnetic properties, leading for instance

Z. Rao, Dr. F. Körmann, Dr. W. Lu, Dr. X. Zhou, Dr. C. Liu, Dr. A. K. da Silva, Dr. D. Ponge, Dr. B. Gault, Prof. J. Neugebauer, Prof. D. Raabe, Prof. Z. Li
Max-Planck-Institut für Eisenforschung
Max-Planck-Straße 1, 40237 Düsseldorf, Germany
E-mail: w.lu@mpie.de

Dr. B. Dutta, Dr. F. Körmann
Department of Materials Science and Engineering
Delft University of Technology
CD Delft 2628, The Netherlands

The ORCID identification number(s) for the author(s) of this article can be found under https://doi.org/10.1002/adfm.202007668.

DOI: 10.1002/adfm.202007668

Dr. W. Lu
Department of Mechanical and Energy Engineering
Southern University of Science and Technology
Shenzhen 518055, China

Dr. U. Wiedwald, Dr. M. Spasova, Prof. M. Farle
Faculty of Physics and Center for Nanointegration
University of Duisburg-Essen
47057 Duisburg, Germany

Dr. B. Gault
Department of Materials
Royal School of Mine
Imperial College London
Prince Consort Road, London SW7 2BP, UK

Prof. Z. Li
School of Materials Science and Engineering
Central South University
Changsha 410083, China
E-mail: lizhiming@csu.edu.cn

to brittle intermetallic precipitates,[5] grain boundary phase formation[4] or precipitates for strength increase following the Orowan effect.[6]

Here, we target phase decomposition of a HEA to intentionally trigger spinodal decomposition for tailoring magnetic properties. Spinodal decomposition is a phase separation reaction happening in a homogenous, supersaturated, and hence metastable phase. It does not involve nucleation but the free energy of the system is spontaneously reduced under energy gain through isostructural chemical decomposition.[7] The two formed regions, with initially identical crystal symmetry but different composition, form spontaneously and progressively. They result from small initial compositional fluctuations that grow into compositional modulations that follow the spinodal lines.[8] The lattice coherency among the adjacent spinodal regions is maintained during the early stages of this transformation pathway. This allows to study and exploit their chemical and structural states under the effect of the resulting compressive or tensile coherency stresses, which derive from Eshelby-type constraints between decomposition zone and matrix. The direction and magnitude of the coherency stresses depend on the volume misfit among the spinodal regions and their surrounding matrix as well as their shapes.

While the effect of hydrostatic and chemical pressure (e.g., via substitutional alloying) on the magnetic properties has been recently studied,[9] the role of spinodal decomposition in this context remains unexplored. As spinodal decomposition is accompanied by the build-up of elastic coherency strains and stresses, as explained above, the resulting pressure and volume changes can be used for adjusting local thermodynamic states. More specifically, volume expansion of a particular phase, relative to its free-standing counterpart, created by hydrostatic tensile stresses, creates a state which is otherwise inaccessible in the design of bulk phases.[10] This is exploited as a key idea in the present study: the many chemical degrees of freedom offered by the HEA concept, compared to conventional alloys, are beneficial to i) chemically design appropriate spinodal regimes; ii) realize the magnitude and direction (compressive/tensile) of the elastic distortion and the associated Hooke stresses of the decomposing spinodal phase(s) and the remaining matrix; and iii) tailor the magnetic features of the spinodal phase(s). Spinodal decomposition in HEAs and related multicomponent alloys thus opens a novel route to realize materials with well-tailored internal elastic distortion states and magnetic properties via the design of coherent multiple phase arrays.

Spinodal decomposition in HEAs was reported before[1c,g,11] but only in confined and segregated regions such as in the Cr-Fe-Co enriched dendrites of an equiatomic AlCoCrCuFeNi alloy[11a] or at the grain boundaries of an equiatomic CoCrFeMnNi alloy.[11b] Moreover, most of these works did not unveil the associated thermodynamics and temporal evolutions of the spinodal. Since the decomposition effects previously observed in HEAs only occurred in spatially confined and segregated lattice defect regions, detailed or systematic observations regarding possible associated improvements in mechanical, electrical, or magnetic behavior were not conducted. For instance, spinodal decomposition phenomena observed in the zones between the primary solidification dendrites in an AlCoCrCuFeNi HEA were observed to increase the saturation magnetization by 9% at ambient temperature.[12] These findings indicate that spinodal decomposition might be a suited design vehicle to enhance the magnetic properties of HEAs as will be demonstrated in this paper.

In this work we compose a novel non-equiatomic $Fe_{15}Co_{15}Ni_{20}Mn_{20}Cu_{30}$ (at. %) HEA by bulk spinodal decomposition upon annealing at 600 °C for 240 h. We find a dramatic increase in Curie temperature by 48%, that is, from 201 K to ambient temperature, and also in magnetization by 20%, 24%, and 70% at 5, 150 K, and ambient temperature, respectively. In situ and ex situ scanning transmission electron microscopy (STEM) and atom probe tomography (APT) were combined to elucidate the temporal evolution of the chemical compositions and the associated thermodynamics with progressing spinodal decomposition. Our results present a novel strategy to design metastable HEAs with outstanding functional properties.

2. Results and Discussion

Spinodal decomposition is effective for tailoring the mechanical and magnetic properties. It benefits from an uphill diffusion process that can be used to create nanoscale dispersed phases with coherent interfaces in otherwise conventional alloys.[13] In previous studies, HEAs have been proven to achieve excellent mechanical properties via confined spinodal decomposition.[1c,g] However, research about tailoring magnetic properties of HEAs via spinodal decomposition is rare. Here, we show how to tailor the magnetic properties of HEAs by using bulk spinodal decomposition.

2.1. Design and In Situ Characterization of HEAs with Spinodal Decomposition

Predicting HEA compositions that are prone to undergo a spinodal decomposition in the bulk is challenging when considering that only a few quaternary or quinary experimental phase diagrams are known. In this work, we used the ThermoCalc 2019 software to calculate the range of temperatures in which the $Fe_{15}Co_{15}Ni_{20}Mn_{20}Cu_{30}$ HEA will undergo a spinodal decomposition, using the TCHEA3 thermodynamic database for HEAs.[14] **Figure 1**a,b shows the thermodynamic calculation results obtained for the $Fe_{15}Co_{15}Ni_{20}Mn_{20}Cu_{30}$ HEA. Figure 1a shows that a phase decomposition trend occurs below 830 °C and a spinodal decomposition below 730 °C, that is, where the stability function changes its sign. Figure 1b shows that Fe, Co, Ni, and Mn are enriched in phase 1 while Cu partitions into phase 2 below 800 °C. This trend of the elemental decomposition behavior predicted by the thermodynamic calculations is consistent with the experimental results shown below but the compositions are not exactly the same. This is attributed to the fact that the used database (TCHEA3) has only been recently developed and might still require refinement, as particularly the magnetic effects are challenging to be correctly captured by such thermodynamic database methods.

To monitor the real-time spinodal decomposition of the $Fe_{15}Co_{15}Ni_{20}Mn_{20}Cu_{30}$ HEA at near-atomic level, we investigated this alloy using in situ heating in the STEM. Prior to in situ probing the bulk samples were first heated to 1000 °C with the

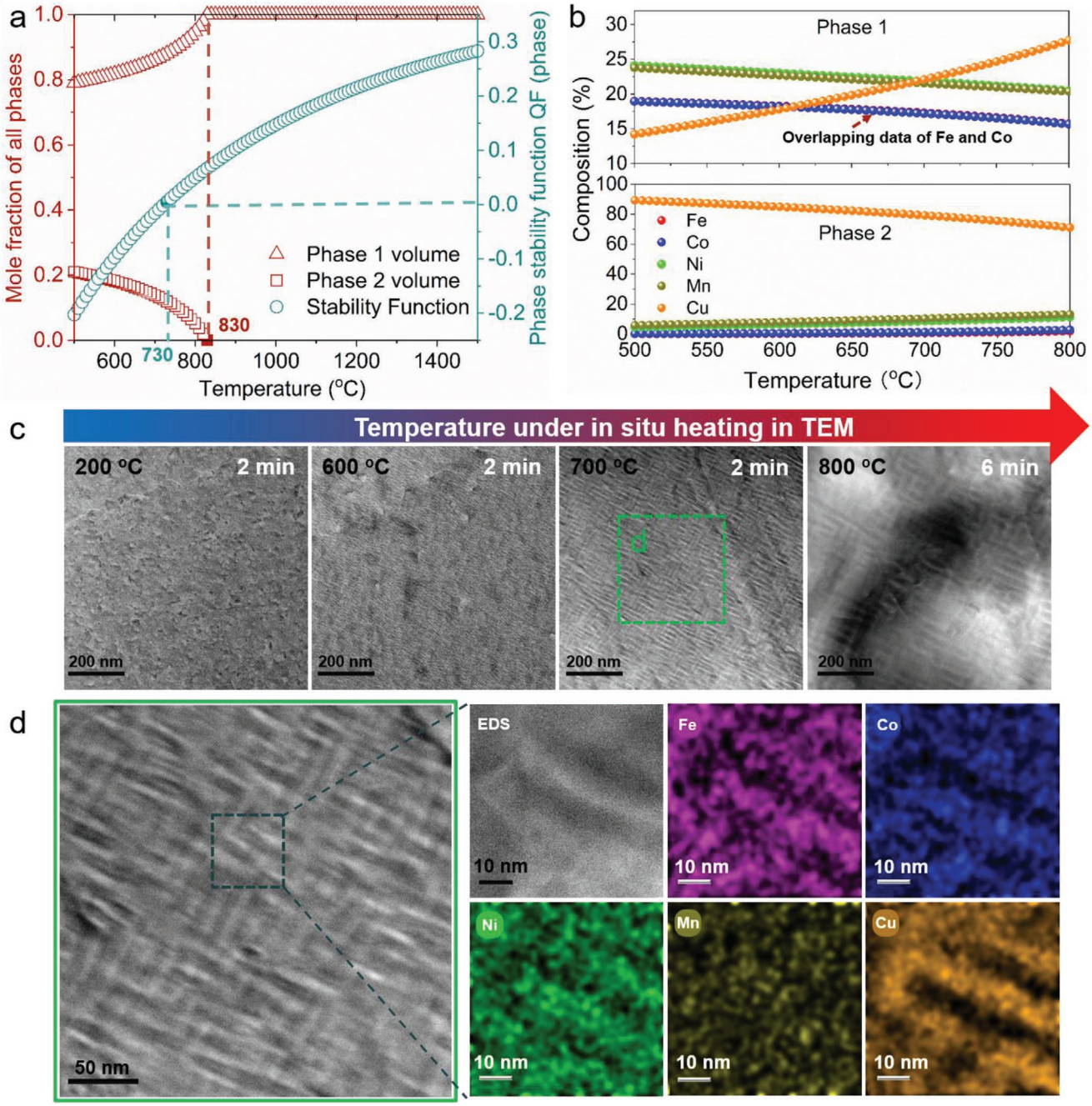

Figure 1. Thermodynamics and in situ observation of spinodal decomposition in a $Fe_{15}Co_{15}Ni_{20}Mn_{20}Cu_{30}$ HEA. a) Calculated mole fraction of the two phases and stability function for the $Fe_{15}Co_{15}Ni_{20}Mn_{20}Cu_{30}$ HEA. Red squares and triangles indicate the mole fraction of the two phases as a function of temperature. The phase stability function, which describes the local curvature of the free energy curve, assumes a negative value if the phase composition is inside of a spinodal region. b) Calculated compositions of the two phases as a function of temperature. Fe, Co, Mn, and Ni are enriched in phase 1 while Cu is enriched in phase 2. The data of Fe (red) and Co (blue) are overlapping in the picture. The thermodynamic calculations were conducted using the Thermo-Calc software in conjunction with the TCHEA3 database. c) Temperature-resolved HAADF-STEM images of the spinodal decomposition of the $Fe_{15}Co_{15}Ni_{20}Mn_{20}Cu_{30}$ HEA annealed in situ at 200, 600, 700 °C for 2 min and 800 °C for 6 min, respectively. d) Enlarged region marked by the short-dashed rectangle in (c) showing a high magnification HAADF-STEM image at 700 °C with corresponding EDS maps of the five principal elements, that is, Fe, Co, Ni, Mn, and Cu, in the same sample region.

aim to form a completely homogeneous solid–solution and then fast cooled to room temperature by water quenching, resulting in a super-saturated solid–solution. Subsequently, TEM specimens were prepared from the bulk samples, and annealed from 200 to 800 °C in situ in the STEM mode to monitor the formation and growth of the compositionally modulated spinodal decomposition features. Figure 1c shows the high-angle annular dark-field (HAADF)-STEM images of the alloy after annealing at

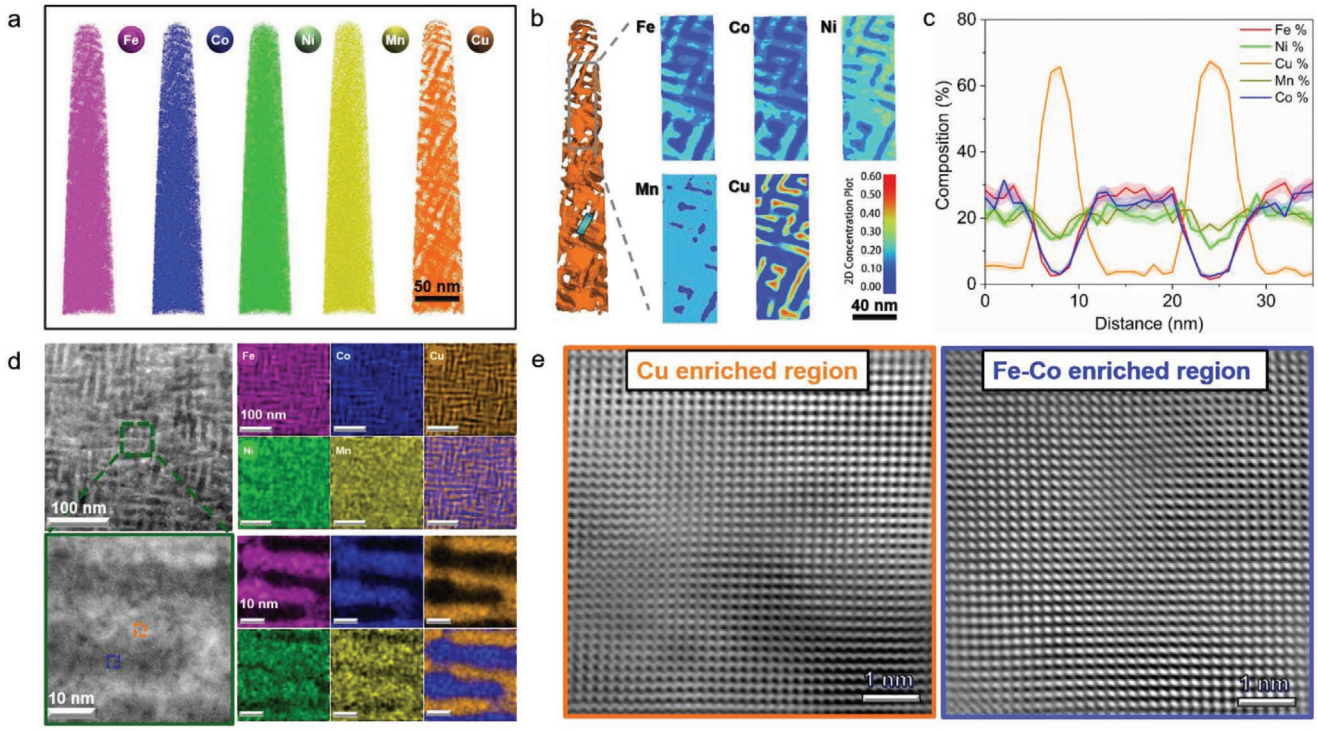

Figure 2. APT and STEM analysis of the homogenized $Fe_{15}Co_{15}Ni_{20}Mn_{20}Cu_{30}$ HEA annealed at 600 °C for 6 h. a) APT tip reconstructions of Fe, Ni, Co, Mn, and Cu. b) 50 at% iso-concentration surfaces of Cu and in-plane compositional analysis of the identical sample region marked on the iso-concentration surfaces. c) 1D compositional profiles taken along the length direction of the cylinder presented in the 50 at% iso-composition surfaces of Cu. d) High and low magnification HAADF-STEM images with corresponding EDS maps. The area of high magnification image is indicated by dark green dashed rectangle in the low magnification image. e) HR-STEM images of the Cu enriched region and the Fe-Co enriched region marked in (d) by the orange dashed rectangle and the blue dashed rectangle, respectively.

200, 600, 700 °C for 2 min and 800 °C for 6 min, respectively. All the images are taken along the <001> zone axis since the spinodal structures in this alloy are formed along {100} habit plane. No traces of the typical morphology of the spinodal decomposition can be observed in the alloy at a temperature of 200 °C, due to suppressed kinetics. When increasing the temperature to 600 °C, wavy and irregularly percolating regions appear as two distinct regions with bright and dark contrast, respectively. When the temperature is further increased to 700 °C, the features grow into typical modulated structures, characteristic of spinodal decomposition, into interconnected patterns. When increasing the temperature to 800 °C, the spacing between the interconnected spinodal regions becomes wider, indicating competitive coarsening. To observe the modulated regions in more detail, Figure 1d shows a HAADF-STEM image of the area marked by the green dash rectangle in Figure 1c. The enlarged image reveals that the two regions have similar volume fractions and their average spacing follows a wavelength of about 20 nm. STEM energy-dispersive spectroscopy (EDS) maps are taken from a small area of 60 × 60 nm^2 marked by a dark green dashed rectangle in Figure 1c. The EDS maps clearly reveal the pronounced redistribution of the five principal elements during the decomposition. The bright region caused by Z-contrast in the STEM image is enriched in Cu while Fe and Co are repelled to another dark-contrast region. The spatial variations of Mn and Ni are smaller than the ones of the other three elements, that is, Fe, Co, and Cu.

The effect of such elemental distribution on the corresponding magnetic properties of the HEA is discussed below in Section 2.3.

2.2. Evolution of Size and Morphology of the Spinodal Patterns

We performed an isothermal annealing from 2 to 240 h at 600 °C in order to investigate the decomposition mechanism and exploit its potential for tailoring the magnetic properties of the material. **Figure 2** shows the APT and STEM results of the $Fe_{15}Co_{15}Ni_{20}Mn_{20}Cu_{30}$ HEA annealed at 600 °C for 6 h. The APT results are presented in terms of 3D (Figure 2a), 2D (Figure 2b), and 1D (Figure 2c) reconstructions to reveal the morphology and elemental distribution during spinodal decomposition. Modulated regions can be observed by the 3D reconstructions of Fe, Co, and Cu in Figure 2a. Figure 2b reveals the 50 at% iso-concentration surfaces of Cu and an in-plane compositional analysis of the identical sample region marked on the iso-concentration surfaces. The in-plane compositional analysis suggests that Cu is repelled by Fe, Co while Ni and Mn slightly partition to the Fe-Co enriched region. Figure 2c shows the corresponding 1D compositional profile taken along the length direction of the cylinder marked in Figure 2b. Cu enriched and Fe-Co enriched regions can be clearly distinguished in terms of the composition modulation. In the Cu enriched region, Cu has a maximum concentration above 60 at% while Fe and Co are

depleted with minimum concentrations below 5 at%. The concentrations of Ni and Mn in this region are slightly below those in the bulk nominal composition. In the Fe-Co enriched region, Fe and Co are around 25 at% while the Cu content is only around 5 at%. It is interesting to note that Ni and Mn are also not uniformly distributed and prone to segregate to the Fe-Co enriched region. This is consistent with the TEM-EDS mapping results shown in Figure 1d. Figure 2d demonstrates the highly-interconnected structures observed by HAADF-STEM at both, high and low magnifications. The spinodal decomposition patterns in the HEA sample have an equiaxed shape and are crystallographically aligned along the <100> directions because of the small coherency-strain energy associated with these directions.[8] The wavelength of the Cu enriched region observed in the HAADF-STEM is around 15 nm, consistent with the results from the APT analysis. Figure 2e shows the high-resolution STEM (HR-STEM) images of the Cu enriched region and the Fe-Co enriched region, which are marked in Figure 2d by the orange and blue dashed rectangle, respectively. The HR-STEM images reveal that the two coherent regions both have FCC structure.

Figure S1, Supporting Information presents the electron backscatter diffraction maps and APT analysis results of the homogenized $Fe_{15}Co_{15}Ni_{20}Mn_{20}Cu_{30}$ HEA. The homogenized alloy is fully recrystallized in the FCC structure. Cu enriched zones are revealed using a set of iso-composition surfaces with a threshold value at 50 at% Cu. The Cu enriched zones embedded in the matrix have an average diameter of 2.94 nm with a volume fraction of 0.86%. These Cu enriched zones reveal the early stage of decomposition occurring already during quenching after the 1000 °C homogenization treatment.[13d] Figure S2, Supporting Information shows the APT analysis results of the HEA sample annealed at 600 °C for 2 h. Compared to the homogenized alloy sample, the 600 °C/2 h annealed sample has higher volume fraction of Cu enriched zones (i.e., 2.7%). Figure S3, Supporting Information reveals the 3D reconstructions of Fe, Co, Ni, Mn, and Cu of the alloy samples annealed at 600 °C for 24 and 240 h. For the samples exposed to a prolonged annealing time (e.g., 240 h), the modulated regions assume larger wavelengths.

Figure 3a shows the combined 1D compositional profiles taken from the APT reconstructions of the $Fe_{15}Co_{15}Ni_{20}Mn_{20}Cu_{30}$ HEA samples with different annealing time at a constant annealing temperature of 600 °C. These profiles have been corrected by using an analytical model[15] to account for the possible overlap caused by local magnifications associated

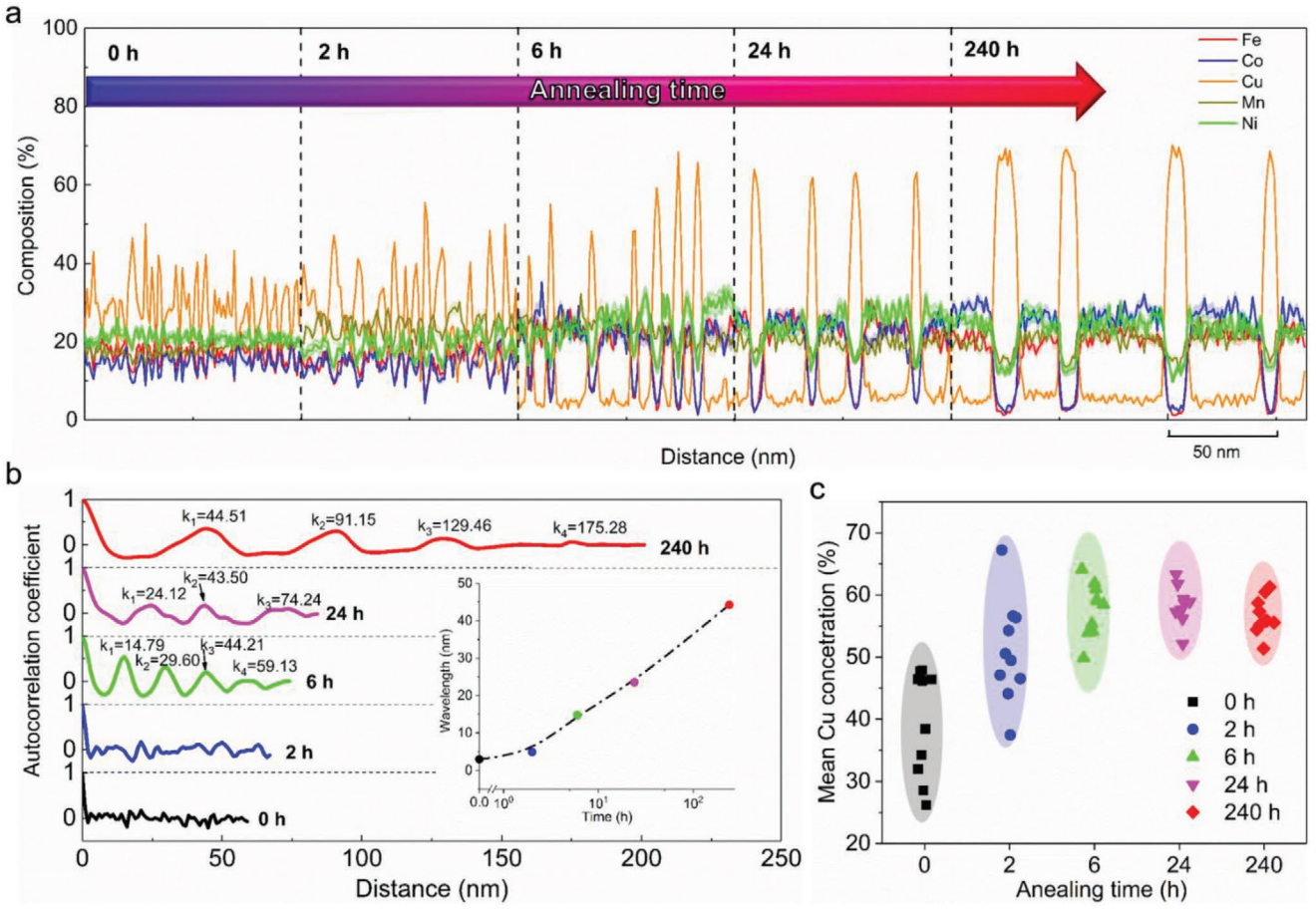

Figure 3. Wavelength and amplitude evolutions of the spinodal decomposition features in the $Fe_{15}Co_{15}Ni_{20}Mn_{20}Cu_{30}$ HEA with increasing annealing time at 600 °C. a) 1D compositional profiles at different annealing times taken from the cylinders with longitudinal directions along <100>. b) Corresponding autocorrelation coefficient profiles of Cu in the 1D compositional profiles presented in (a). The calculated wavelength as a function of annealing time is shown in the inset. c) Evolution of the local Cu concentration in the Cu enriched region in alloy samples annealed at different times.

to differences in the field evaporation behavior of the different phases. With increasing annealing time, the compositional differences between the Cu enriched region and the Fe-Co enriched region become stronger and the wavelength of the compositional modulations becomes wider. As a consequence, the magnetic properties of the HEA can vary significantly due to different annealing time which should be chosen appropriately to achieve optimal properties. Figure 3b reveals the corresponding autocorrelation coefficient profiles[16] extracted from the 1D compositional profiles of Cu in Figure 3a. These reveal the increase of amplitude and wavelength of the spinodal decomposition with increasing annealing time. The parameter k_i is the position of the ith Cu peak. The mean wavelength is calculated as the averaged values k_i/i, i = 1–5.[16,17] The exact wavelength as a function of annealing time is presented in the inset. The wavelength monotonically increases from 2.94 to 44.26 nm with increasing annealing time from 0 to 240 h. The competitive coarsening kinetics, which becomes visible through the changing spacing λ among the spinodal decomposition zones, can be approximated by using the classic Lifshitz–Slyozov–Wagner theory, which is a mean-field model for the kinetics of precipitation and Ostwald ripening from supersaturated solid solutions.[18] The relationship of the wavelength λ as a function of time t evolves as $\lambda \propto t^{1/3}$ during coarsening. Figure 3c shows the evolution of the local Cu concentration in the Cu enriched region as a function of annealing time. Ten measurements of the Cu concentration were obtained for alloy samples annealed from 0 to 240 h. The methods for this are described in Figure S4, Supporting Information. The local Cu concentration plots show that the amplitude of the spinodal decomposition reaches its equilibrium state after 6 h at 600 °C.

2.3. Magnetic Properties from Experiments and Ab Initio Calculations

Figure 4a presents the temperature dependent magnetization of the homogenized $Fe_{15}Ni_{15}Co_{20}Mn_{20}Cu_{30}$ HEA upon heating from 5 to 390 K in an external field ranging from 0.005 to 0.05 T. The solid curves were recorded after zero-field cooling while the dashed curve was measured after 0.5 T field cooling. The curves measured at lower magnetic fields (i.e., 0.005 and 0.01 T) reveal a sharper drop of magnetization compared to that measured at higher magnetic fields (i.e., 0.02 and 0.05 T). We determine the Curie temperature T_c = 201 K of the alloy at the lowest point of the derivatives of the temperature dependent magnetization. The HEA sample annealed at 600 °C for 240 h with spinodal decomposition exhibits a substantially enhanced Curie temperature of 303 K, that is, a 48% increase (Figure 4b). The temperature dependencies of the magnetization curves for three intermediate annealing steps, that is, for 2, 6, and 24 h are shown in Figure S5, Supporting Information. Figure 4c shows the hysteresis loops up to 2 T of the $Fe_{15}Co_{15}Ni_{20}Mn_{20}Cu_{30}$ HEA with different annealing time at 300 K. The magnetization of the HEA sample annealed for 240 h with spinodal decomposition increases by 70% (from 12 to 21 $Am^2\ kg^{-1}$) as compared to the homogenized counterpart (0 h). The hysteresis loops of the HEA up to 2 T at 5 and 150 K, exposed to different annealing times, are shown in Figure S4, Supporting Information. The total magnetization for HEA samples prepared with different annealing times also increases with the formation of the modulated spinodal structures. Figure 4d highlights the impact of the different annealing times on the measured Curie temperature of the HEA samples. The APT reconstructions inserted in Figure 4d, all with dimensions of $40 \times 40 \times 200\ nm^3$, include a set of 50 at% Cu iso-composition surfaces, which highlight the morphological evolution of the modulated structures. These results show that the Curie temperature experiences a slight drop after 2 h annealing and then increases to an equilibrium value after 6 h annealing at 600 °C. These results demonstrate that the Curie temperature is strongly related to composition changes of the different regions, as both the Curie temperature and the mean Cu concentration in the Cu enriched region (see Figure 3c) increase toward the equilibrium state after 6 h annealing.

It should be noted that a Cu-Ni-Mn enriched FCC phase and a Fe-Co enriched BCC phase are found at the grain boundaries of the alloy samples annealed at 600 °C for 24 and 240 h, as shown in Figure S6, Supporting Information. The additional XRD peak marked as "unknown phase" in Figure S7, Supporting Information is likely to be caused by this Cu-Ni-Mn enriched FCC phase at the grain boundaries. The effects of the additional grain boundary phases on the temperature dependence of magnetization curves of the alloy samples are shown in Figure S8, Supporting Information. For the alloy samples annealed at 600 °C for 0, 2, and 6 h (Figures S8a–c, Supporting Information), the magnetization is almost 0 when the temperature is above the Curie temperature. However, for the alloy samples annealed at 600 °C for 24 and 240 h (Figures S8d,e, Supporting Information), there is still some remnant magnetization detected when the temperature is above the Curie temperature. This finding suggests that the additional grain boundary phases provide a small contribution to the magnetization since they are still ferromagnetic when the temperature is above the Curie temperature determined by the Fe-Co enriched spinodal phase. Overall, the additional grain boundary phases have no effect on the Curie temperature of the bulk material but slightly enhance the material's magnetization.

To rationalize the influence of annealing time and spinodal decomposition on the magnetic properties, we calculated the Curie temperatures at the corresponding experimental compositions employing ab initio density functional theory (DFT) simulations. The compositions of the Fe-Co enriched and Cu enriched regions, used in our theoretical simulations, are determined from APT measurements and summarized in Table S2, Supporting Information. Since the diameter of the individual regions are several nanometers (see Figure 2), we treated them in the simulations as bulk-like phases, that is, surface effects between the Fe-Co enriched and Cu enriched regions were neglected. The DFT calculations for the two individual bulk-like systems reveal that the Curie temperature of the Fe-Co enriched region is approximately two times higher than that of the Cu enriched region. This large increase can be attributed to the higher amount of ferromagnetic Fe and Co in the Fe-Co enriched region. For an alloy with co-existing phases, multiple critical temperatures could be defined if some regions of the alloy lose their magnetic ordering at a lower critical temperature. Here we are interested in the highest temperature until

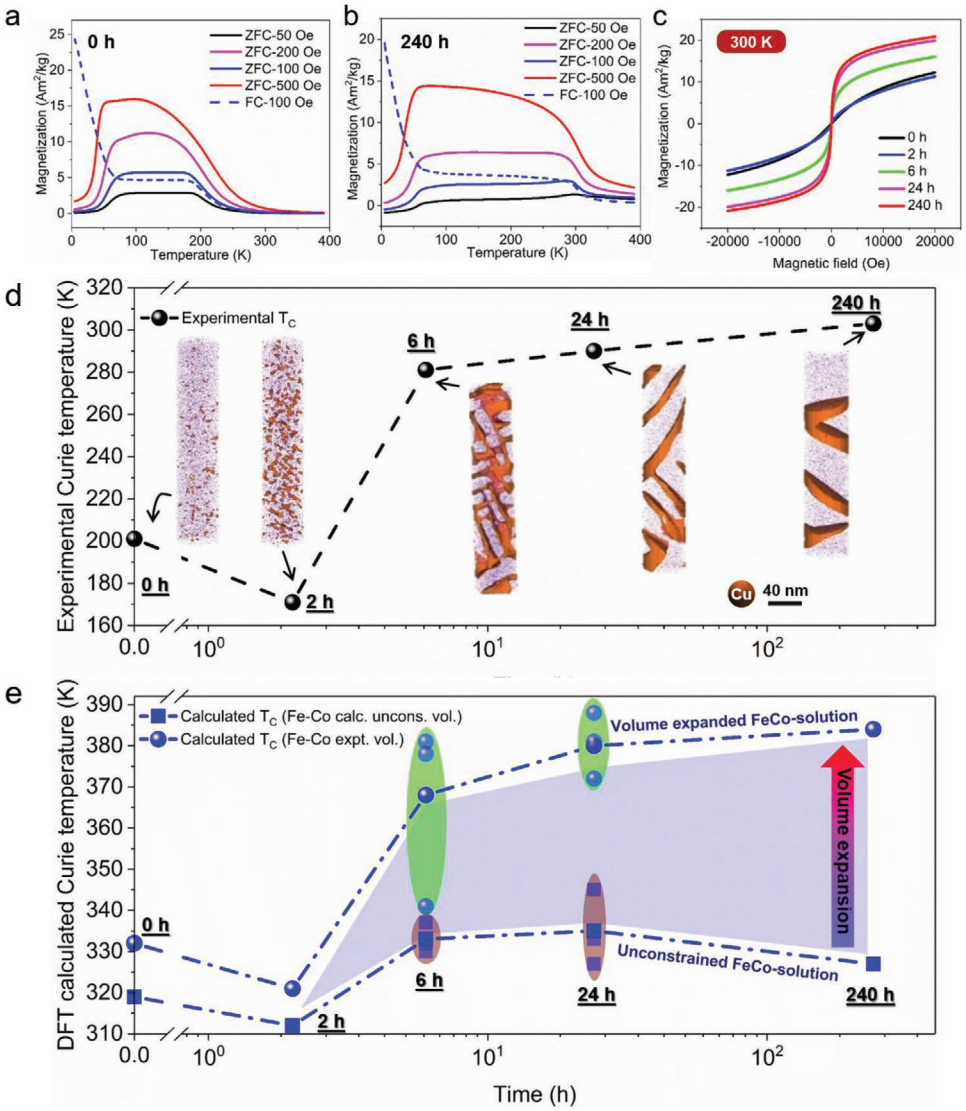

Figure 4. Magnetic properties of the $Fe_{15}Co_{15}Ni_{20}Mn_{20}Cu_{30}$ HEA samples in different processing conditions. a) Temperature dependence of magnetization of the homogenized and b) 600 °C/240 h annealed HEA samples after zero-field cooling in applied magnetic fields of 50-0.05 T and after a 0.5 T field cooling in an applied magnetic field of 0.01 T. c) Hysteresis loops investigated up to 2 T of the HEA with different annealing time at 300 K. d) Experimental Curie temperatures as a function of annealing time. The morphological evolution of the alloy's nanostructure as a function of annealing time is shown in terms of APT reconstructions of volume portions with dimensions of $40 \times 40 \times 200$ nm^3. The APT reconstructions also show 50 at. % iso-composition surfaces of Cu. e) DFT calculated Curie temperatures as a function of annealing time. The blue shaded area indicates the impact of strain induced volume dilatation on the Curie temperature, that is, the difference between the Curie temperature calculated for a hypothetical free-standing unconstrained single-phase bulk-like Fe-Co alloy and that for the experimentally measured strained volume of the same region in the HEA. For the 6 and 24 h annealed samples, light blue squares and spheres indicate the Curie temperature values calculated for compositions corresponding to three different APT tips while the final value is the arithmetic mean over the three compositions. The oval shapes for these two annealing times mark the fluctuations in the Curie temperatures that occur due to the scatter in local composition among the different APT specimens.

which magnetic long-range ordering in the alloy exists, which is determined by the phase with the higher Curie temperature.[19] We therefore determine the Curie temperature of the alloy from the calculated value for the Fe-Co enriched region (see Figure 4e). The computed Curie temperatures are slightly overestimated, a typical feature of the employed mean-field approximation.[20] An advantage of the computational study is that the impact of volume changes of the individual phases can be systematically studied. For a single-phase FeCoNiMnCu alloy,[21] we have estimated the Curie temperature at the alloys' equilibrium volume. In the present study, however, the spinodal decomposition leads to regions with different compositions and, potentially, different local volumes due to coherency stresses, each capable of affecting magnetic properties such as the Curie temperature. To evaluate the volume effect, we performed DFT calculations for the APT measured compositions and computed the volume of a hypothetically free-standing (unconstrained) Fe-Co solid solution (see also Figure S9, Supporting Information). We find that the relaxed equilibrium volume of this Fe-Co region in the unconstrained bulk-like state

would decrease by ≈3.2% after 240 h of annealing with respect to the volume of the 0 h annealed HEA. In contrast, however, the XRD measurement (shown in Figure S6, Supporting Information) for the HEA after 240 h of annealing exhibit only a 1.1% reduction in volume of the Fe-Co enriched region. This suggests a tensile hydrostatic coherency strain acting on the Fe-Co enriched region, caused by the Cu enriched region. We estimated the lattice misfit of the current alloys based on Svoboda's scheme[22] for calculating the stress created by two adjacent coherent phases in superalloys.[23] The lattice misfit δ is defined as $\delta = 2(a_\gamma - a_{\gamma'})/(a_\gamma + a_{\gamma'})$, where a_γ and $a_{\gamma'}$ are the lattice parameters of the two adjacent FCC phases. For the alloy annealed at 600 °C for 240 h, the lattice misfit is around 0.37% and the associated lattice misfit stress is estimated to be around 375.9 MPa. Additionally, we also derived the volumetric strain, that is, (change in volume/original volume) × 100%, for the Fe-Co region which is in the range of ≈1.5% to 4% depending on the considered alloy (see Table S3, Supporting Information). To study the impact of such a volume effect on the Curie temperature, we simulate the Curie temperature of the Fe-Co enriched region not only using the experimentally measured volume, but also using the volume of the hypothetical isolated strain-free Fe-Co bulk-like phase. Figure 4e shows the calculated Curie temperatures of the Fe-Co enriched region at these two different volumes, that is, at the equilibrium volume of the Fe-Co enriched region as a hypothetically single phase strain-free (marked with blue squares) and at the experimentally measured volume of this region in the decomposed alloy (marked with blue spheres). Note that for the 6 and 24 h annealed samples, Curie temperatures were calculated for three slightly different compositions (marked with light blue squares and spheres), corresponding to the compositions yielded for the three different APT tips with the final value being the arithmetic mean over the three compositions. This allows us to investigate the fluctuations in the calculated Curie temperatures (ovals) that occur due to the uncertainty in composition of the APT analysis. Such compositional uncertainties and thus fluctuations in the computed Curie temperature could also occur for the other considered annealing times. Such fluctuations are, however, not large enough to alter the main trend derived from the calculated Curie temperatures.

The calculated trend for the Curie temperature at the experimentally measured volume of the Fe-Co enriched region (which is under tensile hydrostatic strain as compared to its hypothetical single-phase unconstrained counterpart) correctly describes the experimentally observed changes in Curie temperature versus annealing time. Since the experimentally measured volume change is small (≈1.1%), the strong increase in the Curie temperature of about 60 K is governed by the chemical composition of the Fe-Co enriched region, in particular the increase of the Fe- and Co-amount, see Table S2, Supporting Information). In contrast, the time evolution of the Curie temperatures calculated for a hypothetical strain-free single-phase Fe-Co solid solution (with the same composition) shows a qualitatively very different trend. The increase of Curie temperature in this case after 240 h of annealing is below 8 K. This much weaker increase of the Curie temperature is caused by the decreasing volume of this phase, if it would be a strain-free single-phase bulk-like material. This clearly shows that the remarkably increased Curie temperature as obtained in the present HEAs after prolonged annealing cannot be explained by the formation of the Fe-Co enriched region without considering some elastic strain. Rather, the tensile hydrostatic strain of ≈2% caused by the Cu enriched region, translating to the volume expansion of the Fe-Co enriched region is central to achieve the improved magnetic properties. Thus, the spinodal decomposition in the present HEA provides an ideal platform to constrain the decomposed regions (in this case Fe-Co enriched region at an expanded volume as compared to its strain-free state) thereby improving the overall alloys' magnetic properties. Due to the presence of multiple principal elements, miscibility gaps in HEAs can be well tailored for triggering spinodal decomposition. Hence, the present approach of using the miscibility gap to purposefully trigger spinodal decomposition is a promising strategy to tailor functional properties of HEAs and other multicomponent alloys, as demonstrated here for the example of magnetism.

3. Conclusions

In conclusion, we show for a prototypical non-equiatomic metastable FeCoNiMnCu HEA that spinodal decomposition can be used to design a specific Fe-Co enriched region at an expanded volume (due to coherency stresses) to improve the alloys' magnetic properties, relative to those for an unconstrained single-phase bulk-like material of the same composition. We investigated the spinodal decomposition at atomic scale in situ with a heating stage in the TEM. The composition evolution was tracked ex situ by STEM and APT probing. By employing DFT calculations we identify as origin of the large enhancement of the magnetic properties the formation of Fe-Co enriched region which is under a tensile hydrostatic strain, that is, volume dilatation, due to the coherency strains imposed by the surrounding matrix. The multi-component HEA approach provides an ideal platform for designing materials with an adequate spinodal regime owing to its many degrees of freedom regarding both, composition and coherency strains. As a result, the decomposed HEA with two regions (Fe-Co enriched region and Cu enriched region) leads to a surprisingly large increase in Curie temperature and magnetization.

Thus, we show here that we break the initially advocated limits of stable solid solutions to stabilize HEAs, opening up alternative avenues for the design of advanced functional materials. The new approach is characterized by three measures that violate the original HEA concept: first, we use the wide compositional space of HEAs to render them not stable but instead thermodynamically metastable. Second, the metastable state should be suited to trigger spinodal decomposition. Third, this decomposition should be associated with composition- and coherency-dependent elastic constraints that introduce site- and phase-specific internal stresses as an additional design parameter, here, used for lending the regions affected better magnetic properties.

Supporting Information

Supporting Information is available from the Wiley Online Library or from the author.

Acknowledgements

The kind support of professor M. Acet at the University of Duisburg-Essen, B. Breitbach, F. Schlüter, U. Tezins, A. Sturm, V. Kree, J. Thomas, M. Nellessen, K. Angenendt, C. Bross, M. Adamek, F. Stein, and L. Christiansen at the Max-Planck-Institut für Eisenforschung is gratefully acknowledged. Funding from the German Research Foundation (Deutsche Forschungsgemeinschaft, DFG) within the Priority Programme 2006 (Compositionally Complex Alloys—High Entropy Alloys) and from NWO/STW (VIDI grant 15707) are gratefully acknowledged. The author (Z.R.) would like to acknowledge the financial support from the China Scholarship Council (Number: 201706460026). Z.L. would like to acknowledge the financial support by the National Natural Science Foundation of China (Grant No. 51971248) and the Hunan Special Funding for the Construction of Innovative Province (2019RS1001). This work was also in part supported by the Deutsche Forschungsgemeinschaft—Project-ID 405553726—TRR 270.

Open access funding enabled and organized by Projekt DEAL.

Conflict of Interest

The authors declare no conflict of interest.

Keywords

coherency constraints, density functional theory, high-entropy alloys, magnetic properties, spinodal decomposition

Received: September 8, 2020
Revised: October 27, 2020
Published online:

[1] a) Y. Zhang, T. Zuo, Y. Cheng, P. K. Liaw, *Sci. Rep.* **2013**, *3*, 1455; b) E. P. George, D. Raabe, R. O. Ritchie, *Nat. Rev. Mater.* **2019**, *4*, 515; c) J. W. Yeh, S. K. Chen, S. J. Lin, J. Y. Gan, T. S. Chin, T. T. Shun, C. H. Tsau, S. Y. Chang, *Adv. Eng. Mater.* **2004**, *6*, 299; d) B. Gludovatz, A. Hohenwarter, D. Catoor, E. H. Chang, E. P. George, R. O. Ritchie, *Science* **2014**, *345*, 1153; e) Z. Li, K. G. Pradeep, Y. Deng, D. Raabe, C. C. Tasan, *Nature* **2016**, *534*, 227; f) Z. Lei, X. Liu, Y. Wu, H. Wang, S. Jiang, S. Wang, X. Hui, Y. Wu, B. Gault, P. Kontis, *Nature* **2018**, *563*, 546; g) Y.-J. Liang, L. Wang, Y. Wen, B. Cheng, Q. Wu, T. Cao, Q. Xiao, Y. Xue, G. Sha, Y. Wang, *Nat. Commun.* **2018**, *9*, 4063; h) M. Zhang, Y. Ma, W. Dong, X. Liu, Y. Lu, Y. Zhang, R. Li, Y. Wang, P. Yu, Y. Gao, *Mater. Sci. Eng., A* **2020**, *771*, 138566; i) J. Brechtl, S. Chen, C. Lee, Y. Shi, R. Feng, X. Xie, D. Hamblin, A. M. Coleman, B. Straka, H. Shortt, R. J. Spurling, P. K. Liaw, *Metals* **2020**, *10*, 1101; j) Y. Zhang, T. T. Zuo, Z. Tang, M. C. Gao, K. A. Dahmen, P. K. Liaw, Z. P. Lu, *Prog. Mater. Sci.* **2014**, *61*, 1.

[2] S. Ma, *Mater. Res. Express* **2019**, *6*, 126508.

[3] a) H. S. Oh, D. Ma, G. P. Leyson, B. Grabowski, E. S. Park, F. Körmann, D. Raabe, *Entropy* **2016**, *18*, 321; b) C. Varvenne, A. Luque, W. A. Curtin, *Acta Mater.* **2016**, *118*, 164.

[4] F. Otto, A. Dlouhý, K. G. Pradeep, M. Kuběnová, D. Raabe, G. Eggeler, E. P. George, *Acta Mater.* **2016**, *112*, 40.

[5] J. He, H. Wang, Y. Wu, X. Liu, H. Mao, T. Nieh, Z. Lu, *Intermetallics* **2016**, *79*, 41.

[6] Z. Li, C. C. Tasan, H. Springer, B. Gault, D. Raabe, *Sci. Rep.* **2017**, *7*, 9892.

[7] J. W. Cahn, *Acta Metall.* **1961**, *9*, 795.

[8] G. Kostorz, *Phase Transformations in Materials*, Wiley, New York **2001**.

[9] a) L. Mañosa, X. Moya, A. Planes, O. Gutfleisch, J. Lyubina, M. Barrio, J.-L. Tamarit, S. Aksoy, T. Krenke, M. Acet, *Appl. Phys. Lett.* **2008**, *92*, 012515; b) H. Nakamura, H. Wada, K. Yoshimura, M. Shiga, Y. Nakamura, J. Sakurai, Y. Komura, *J. Phys. F: Met. Phys.* **1988**, *18*, 981.

[10] a) M. Akhlaghi, T. Steiner, S. R. Meka, A. Leineweber, E. J. Mittemeijer, *Acta Mater.* **2015**, *98*, 254; b) M. Akhlaghi, T. Steiner, S. R. Meka, E. J. Mittemeijer, *J. Appl. Crystallogr.* **2016**, *49*, 69.

[11] a) S. Singh, N. Wanderka, B. Murty, U. Glatzel, J. Banhart, *Acta Mater.* **2011**, *59*, 182; b) L. Li, Z. Li, A. K. da Silva, Z. Peng, H. Zhao, B. Gault, D. Raabe, *Acta Mater.* **2019**, *178*, 1.

[12] S. Singh, N. Wanderka, K. Kiefer, K. Siemensmeyer, J. Banhart, *Ultramicroscopy* **2011**, *111*, 619.

[13] a) E. P. Butler, G. Thomas, *Acta Metall.* **1970**, *18*, 347; b) Y. Iwama, M. Takeuchi, *Trans. Jpn. Inst. Met.* **1974**, *15*, 371; c) L. Zhou, W. Tang, L. Ke, W. Guo, J. D. Poplawsky, I. E. Anderson, M. J. Kramer, *Acta Mater.* **2017**, *133*, 73; d) L. Zhou, W. Guo, J. D. Poplawsky, L. Ke, W. Tang, I. E. Anderson, M. J. Kramer, *Acta Mater.* **2018**, *153*, 15; e) I. Baker, R. Zheng, D. W. Saxey, S. Kuwano, M. W. Wittmann, J. A. Loudis, K. Prasad, Z. Liu, R. Marceau, P. Munroe, *Intermetallics* **2009**, *17*, 886.

[14] a) H. Mao, H.-L. Chen, Q. Chen, *J. Phase Equilib. Diffus.* **2017**, *38*, 353; b) H.-L. Chen, H. Mao, Q. Chen, *Mater. Chem. Phys.* **2018**, *210*, 279.

[15] D. Blavette, F. Vurpillot, P. Pareige, A. Menand, *Ultramicroscopy* **2001**, *89*, 145.

[16] a) J. Piller, H. Wendt, in *Proc. of the 29th IFES* (Eds: H.-O. Andrén, H. Nordén), Gothenburg **1982**, p. 265; b) M. Hetherington, M. Miller, *J. Phys. Colloq.* **1987**, *48*, C6; c) C. Dalzell, *J. Phys. Colloq.* **1988**, *49*, C6.

[17] a) J. Emo, C. Pareige, S. Saillet, C. Domain, P. Pareige, *J. Nucl. Mater.* **2014**, *451*, 361; b) B. Zhang, F. Xue, S. Li, X. Wang, N. Liang, Y. Zhao, G. Sha, *Acta Mater.* **2017**, *140*, 388.

[18] a) I. M. Lifshitz, V. V. Slyozov, *J. Phys. Chem. Solids* **1961**, *19*, 35; b) C. Wagner, *Z. Elektrochem.* **1961**, *65*, 581.

[19] a) T. S. Chin, T. S. Wu, C. Chang, *J. Appl. Phys.* **1983**, *54*, 4502; b) S. Huang, Á. Vida, D. Molnár, K. Kádas, L. K. Varga, E. Holmström, L. Vitos, *Appl. Phys. Lett.* **2015**, *107*, 251906.

[20] a) S. Huang, E. Holmström, O. Eriksson, L. Vitos, *Intermetallics* **2018**, *95*, 80; b) S. Mu, J. Yin, G. D. Samolyuk, S. Wimmer, Z. Pei, M. Eisenbach, S. Mankovsky, H. Ebert, G. M. Stocks, *Phys. Rev. Mater.* **2019**, *3*, 014411.

[21] Z. Rao, B. Dutta, F. Körmann, D. Ponge, L. Li, J. He, L. Stephenson, L. Schäfer, K. Skokov, O. Gutfleisch, *Phys. Rev. Mater.* **2020**, *4*, 014402.

[22] J. Svoboda, P. Lukáš, *Acta Mater.* **2000**, *48*, 2519.

[23] H. Long, H. Wei, Y. Liu, S. Mao, J. Zhang, S. Xiang, Y. Chen, W. Gui, Q. Li, Z. Zhang, *Acta Mater.* **2016**, *120*, 95.